Electronic Supplementary Material (ESI) for Chemical Communications.

Chemical evidence of the stability of praseodymium(V) in gas-phase oxide nitrate complexes

Bernardo Monteiro,[a] Nuno A. G. Bandeira,* [b] Célia Lourenço,[a ‡] Ana F. Lucena,[a] José M. Carretas,[a] John K. Gibson[c] and Joaquim Marçalo* [a]

[a] *Centro de Ciências e Tecnologias Nucleares and Centro de Química Estrutural, Instituto Superior Técnico, Universidade de Lisboa, 2695-066 Bobadela LRS, Portugal.*

[b] *BioISI and Centro de Química e Bioquímica, Faculdade de Ciências, Universidade de Lisboa, 1749-016 Lisboa, Portugal.*

[c] *Chemical Sciences Division, Lawrence Berkeley National Laboratory, Berkeley, CA 94720, USA.*

* Email: nuno.bandeira@ciencias.ulisboa.pt; jmarcalo@ctn.tecnico.ulisboa.pt

‡ Present address: *Centre for Environmental and Agricultural Informatics, Cranfield University, Cranfield, Bedfordshire MK43 0AL, UK.*

Supplementary Information

Contents

1. Experimental Details

The QIT-MS experiments were performed using a Bruker HCT equipped with an ESI interface, with MS^n capability and operated in the negative ion accumulation and detection mode. Stock solutions of $Ln^{III}(NO_3)_3(H_2O)_x$ 10^{-2} M in water were diluted with ethanol to prepare 10^{-4} M solutions for ESI. The metal nitrate solutions were directly injected into the capillary in the ESI source using a syringe pump with a flow rate of 150 μL h^{-1}. The spectra were acquired using typical instrumental parameters.[a] The helium buffer gas pressure in the trap was constant at ca. 10^{-4} Torr. The background water pressure in the ion trap is estimated to be of about 10^{-6} Torr. The MS^n capabilities of the QIT were used for isolation of ions with a specific *m/z* and subsequent CID of mass-selected ions, using the helium buffer gas as the collision partner, or for introducing an ion/molecule reaction time of up to 10 s. The helium provides third-body collisions, which remove energy and stabilize product ions after CID, and both thermalize reagent ions and stabilize product ions in ion/molecule reactions. Pseudo-first order reaction rates, *k*, for thermal (~300 K) hydrolysis of trapped ions in the QIT were obtained by isolating the ion of interest and allowing it to react with background water for variable times. Plots of the logarithmic decay of the ratio of the reactant ion intensity to the total ion intensity as a function of time provide the hydrolysis reaction rates. The mass spectrometer has been previously modified to allow for the introduction of gaseous reagents into the ion trap through a variable leak valve,[b] in a configuration similar to one described before in detail;[c] this setup was used for the experiments with higher water pressure.

a. A. F. Lucena, C. Lourenço, M. C. Michelini, P. X. Rutkowski, J. M. Carretas, N. Zorz, L. Berthon, A. Dias, M. C. Oliveira, J. K. Gibson, J. Marçalo, Phys. Chem. Chem. Phys. 2015, 17, 9942.

b. A. F. Lucena, J. M. Carretas, J. Marçalo, M. C. Michelini, Y. Gong, J. K. Gibson, J. Phys. Chem. A 2015, 119, 3628.

c. D. Rios, P. X. Rutkowski, D. K. Shuh, T. H. Bray, J. K. Gibson, M. J. Van Stipdonk, J. Mass Spectrom. 2011, 46, 1247.

2. Additional Spectra

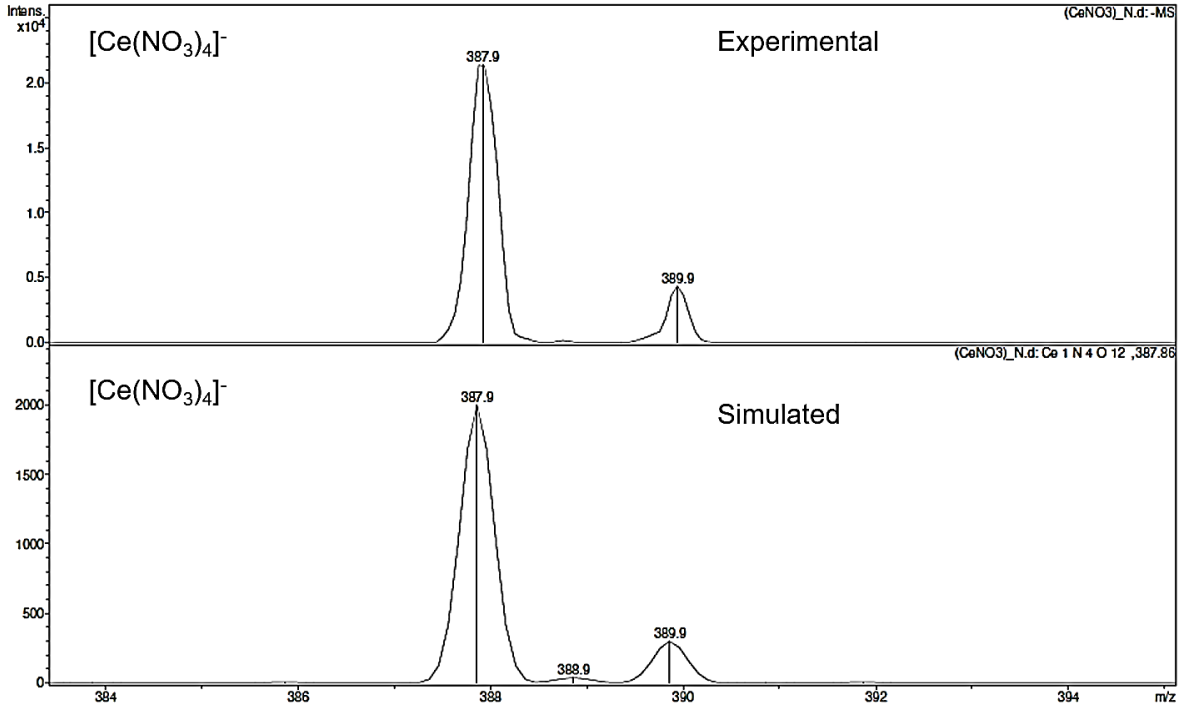

Figure S1– Experimental and simulated isotope pattern of $[Ce(NO_3)_4]^-$ generated by ESI; for subsequent CID experiments, the ion containing Ce-140 at *m/z* 388 was isolated.

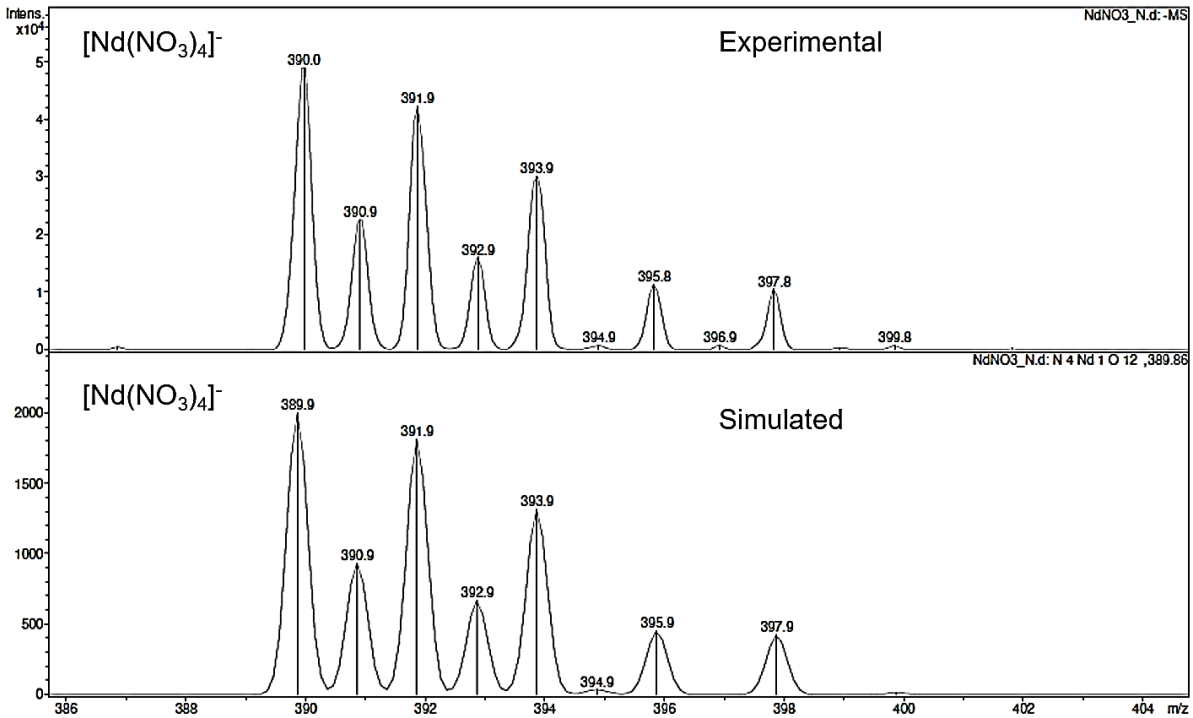

Figure S2– Experimental and simulated isotope pattern of $[Nd(NO_3)_4]^-$ generated by ESI; for subsequent CID experiments, the ion containing Nd-142 at *m/z* 390 was isolated.

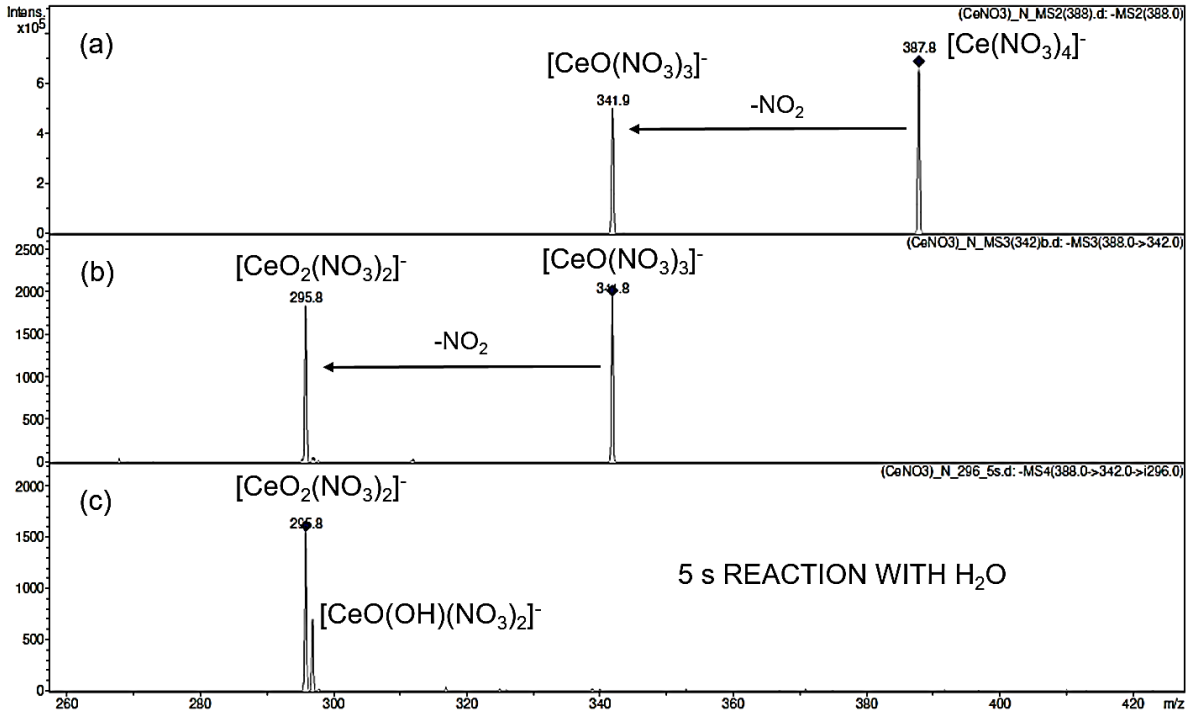

Figure S3 – (a) CID of isolated $[Ce(NO_3)_4]^-$ producing $[CeO(NO_3)_3]^-$; (b) CID of isolated $[CeO(NO_3)_3]^-$ producing $[CeO_2(NO_3)_2]^-$; (c) 5 s reaction of isolated $[CeO_2(NO_3)_2]^-$ with background water to yield $[CeO(OH)(NO_3)_2]^-$.

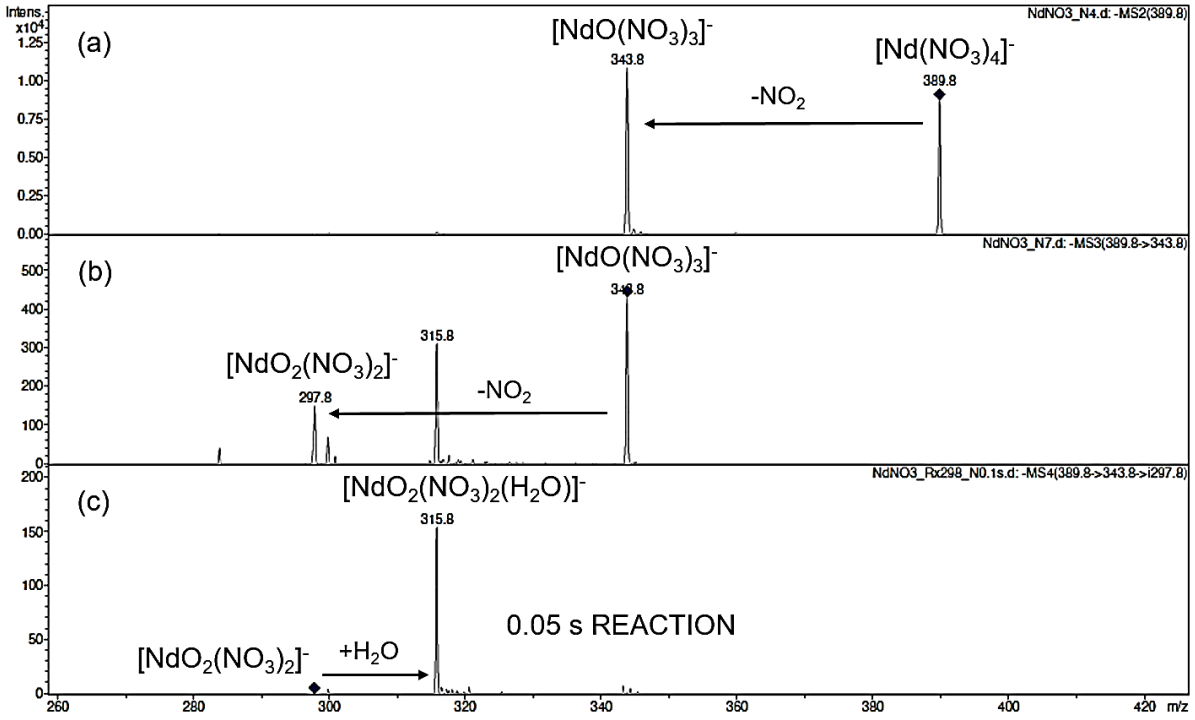

Figure S4 – (a) CID of isolated $[Nd(NO_3)_4]^-$ producing $[NdO(NO_3)_3]^-$; (b) CID of isolated $[NdO(NO_3)_3]^-$ producing $[NdO_2(NO_3)_2]^-$ (to note the presence of a significant peak at *m/z* 316 resulting from the reaction of $[NdO_2(NO_3)_2]^-$ with background water); (c) 0.05 s reaction of isolated $[NdO_2(NO_3)_2]^-$ with background water to yield $[NdO_2(NO_3)_2(H_2O)]^-$.

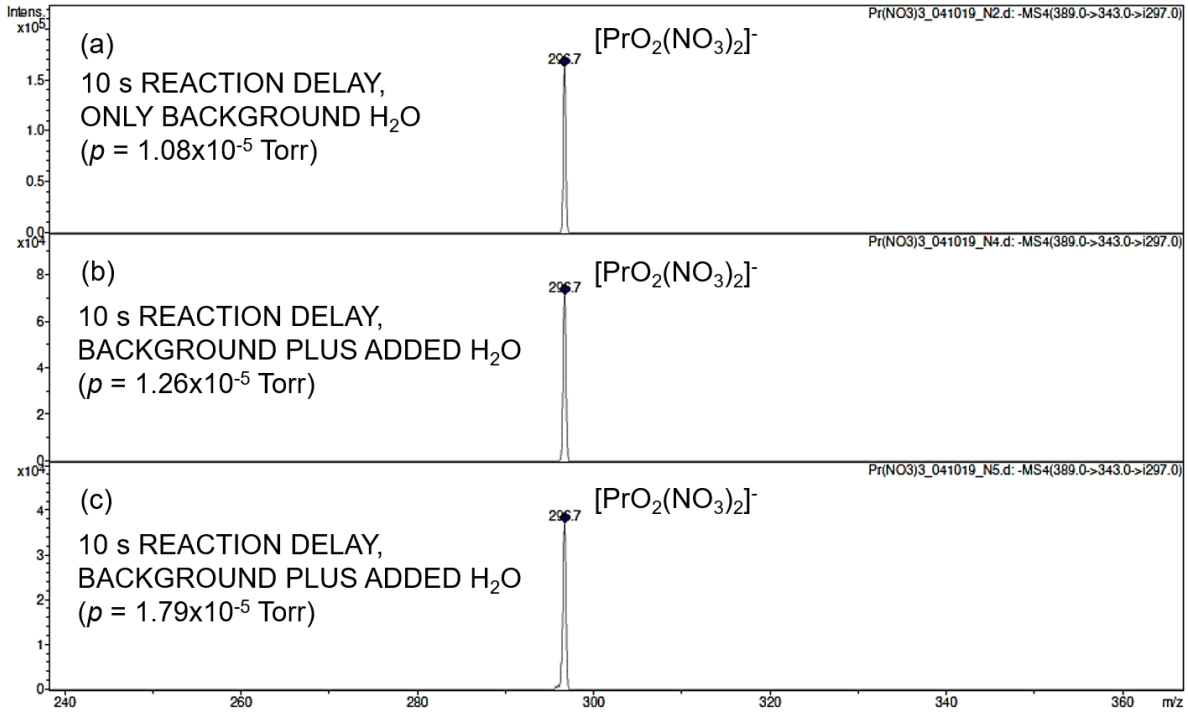

Figure S5 – (a) $[PrO_2(NO_3)_2]^-$ isolated for 10 s in the presence of background water; (b) and (c) $[PrO_2(NO_3)_2]^-$ isolated for 10 s in the presence of background plus added water. The indicated pressure values are the measured total values that include the helium and other background gases.

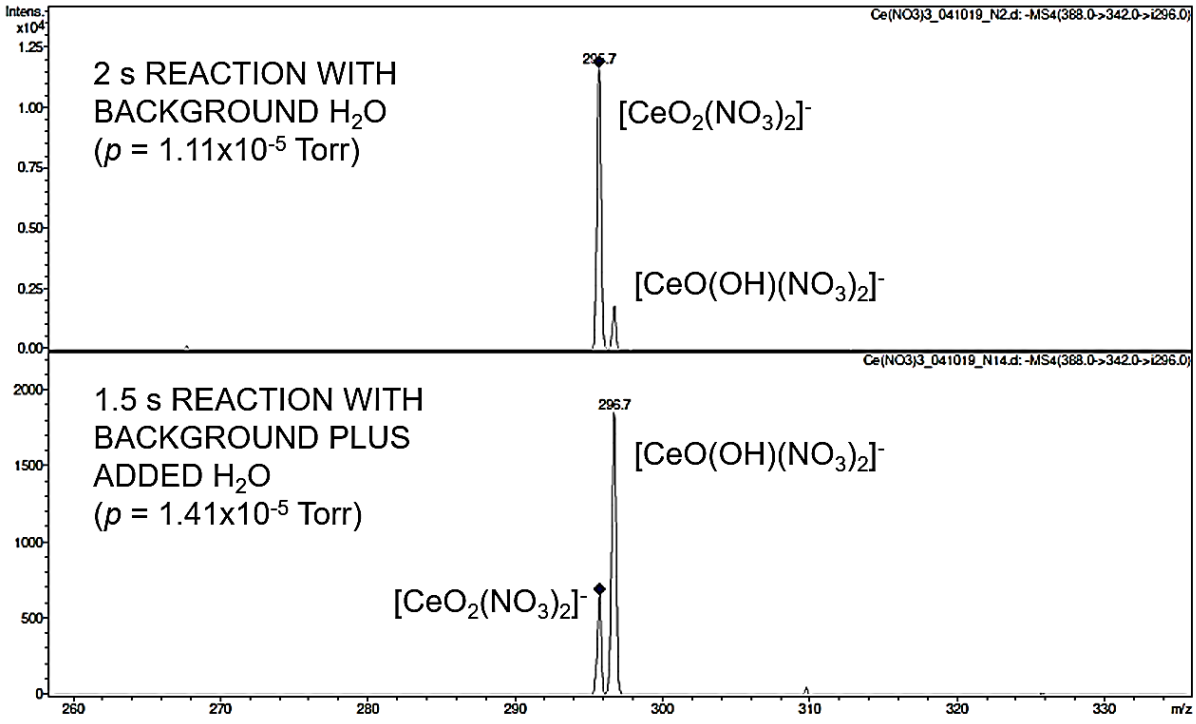

Figure S6 – Reactions of isolated $[CeO_2(NO_3)_2]^-$ with background water (top) and background plus added water (bottom), to yield $[CeO(OH)(NO_3)_2]^-$. The indicated pressure values are the measured total values that include the helium and other background gases.

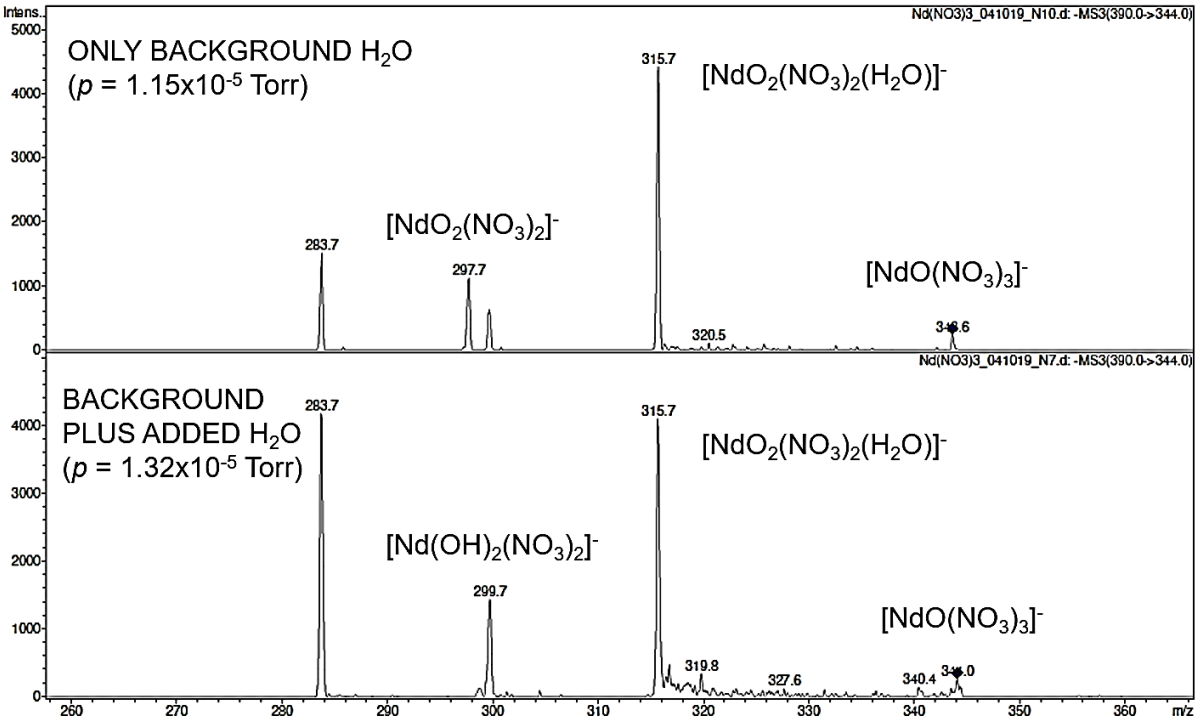

Figure S7 –CID of isolated $[NdO(NO_3)_3]^-$ in the presence of only background water (top) and in the presence of background plus added water (bottom). To note that the peak at *m/z* 298, $NdO_2(NO_3)_2]^-$, is absent in the bottom spectrum due to the reaction with water in larger amount in the ion trap. The indicated pressure values are the measured total values that include the helium and other background gases. The peak at *m/z* 284 results from secondary CID (see Fig. S9).

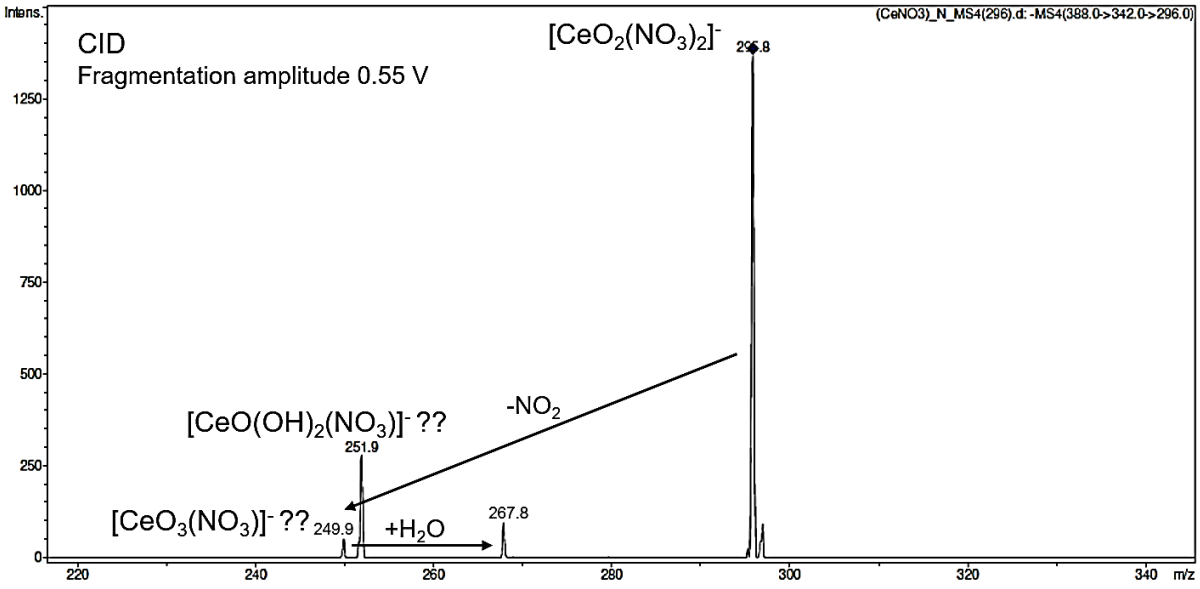

Figure S8– CID of $[CeO_2(NO_3)_2]^-$.

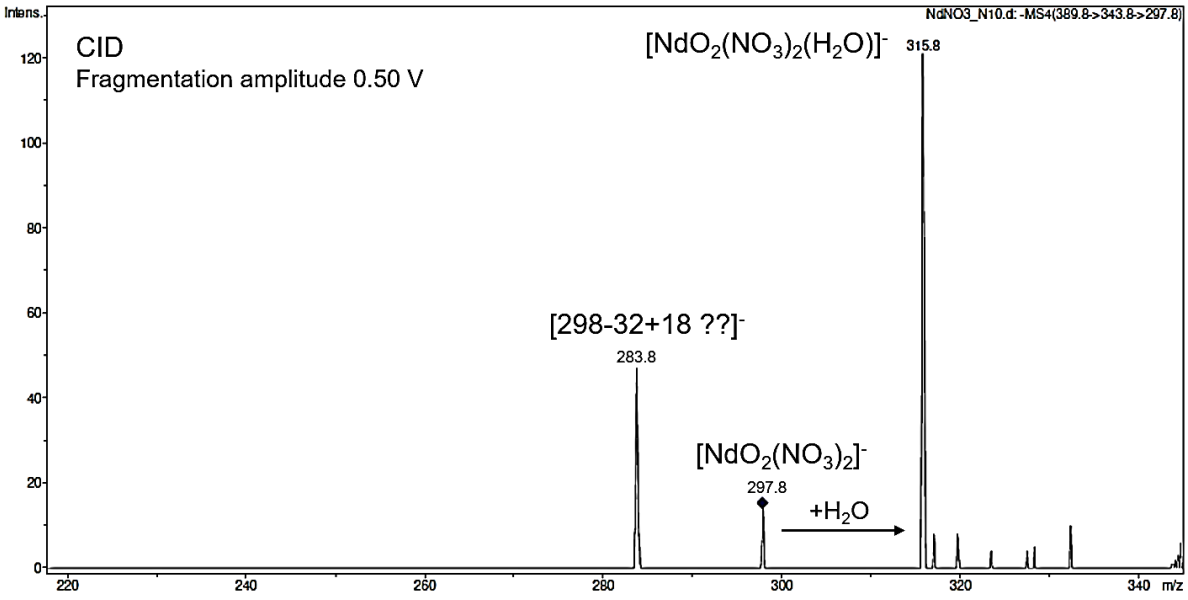

Figure S9 – CID of $[NdO_2(NO_3)_2]^-$.

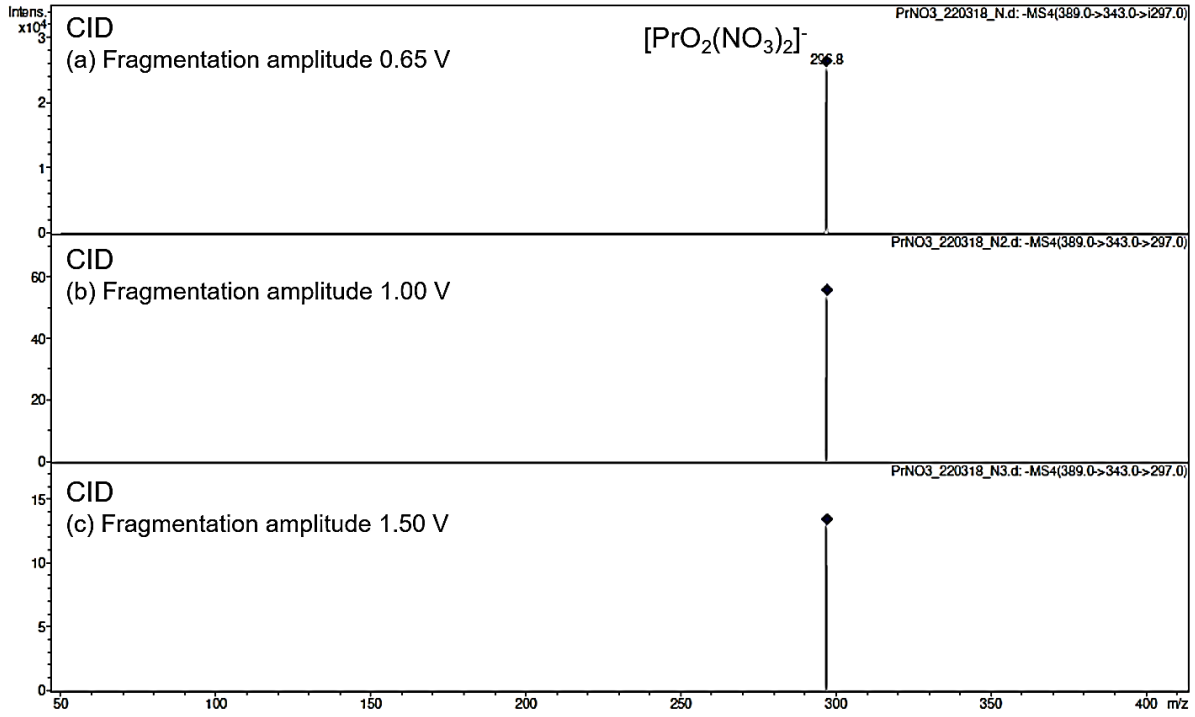

Figure S10 – CID of $[PrO_2(NO_3)_2]^-$ at three increasing fragmentation amplitudes, from (a) to (c), showing a decrease in spectrum intensity and the absence of product ions. MS/MS experiments in a QIT have a low-mass cut-off that depends on the *m/z* of the isolated precursor ion; this limit can be depressed, and so it was down to *m/z* ca. 50, chosen so that fragmentation possibly leading to NO_3^- could be observed, but the detection efficiency at low *m/z* is restricted.

3. Computational Details

All model geometry optimisations were performed using the Møller-Plesset[1] perturbation theory approach to second order with the Resolution of the Identity[2] approximation to multi-centre integrals (RI-MP2) as implemented in the ORCA 4.0 program[3] suite. The spin unrestricted formalism was chosen for the open shell cases and no symmetry constraints were adopted in the optimisations. Relativistic effects were considered with the use of the Zero Order Regular Approximation (ZORA) Hamiltonian with the relevant Segmented All Electron Relativistically Contracted basis sets of triple zeta split valence quality augmented with two polarization functions for the lanthanides (SARC-TZVPP). The lighter elements (O,N,H) employed a standard relativistic triple zeta polarized basis set (ZORA-def2-TZVP). Automatic density fitting auxiliary basis sets were generated for each calculation. A convergence criterion of 10^{-6} was chosen to solve the Z-vector coupled-perturbed SCF equations. The lowest energy isomers of the dioxo structures underwent Hessian analysis to confirm the nature of the stationary point as a local minimum.

For the broken symmetry MP2 outputs spin projection was applied using the Nishino formula[4]

$$E_{LS}\text{-}E_{HS} = \frac{2(E_{BS}\text{-}E_{HS})}{\langle \hat{S}^2 \rangle_{HS}\text{-}\langle \hat{S}^2 \rangle_{BS}} \quad (1)$$

where E_{BS} is the energy of the broken symmetry MP2 energy, E_{HS} the associated high spin multiplet energy and $\langle S^2 \rangle$ the expectation value of the quantum mechanical squared spin operator.

Natural Bond Orbital analysis was carried out via the GENNBO 6.0 program[5] interfaced with the Molden2AIM[6] conversion utility.

A single point Domain based Local Pair Natural Orbital[7] Coupled Cluster with Singles, Doubles and iterated Triples[8, 9] [DLPNO-CCSD(T)] calculation was performed post-optimisation on structures that did not display spin contamination. The residual tolerance for the Coupled Cluster iterations was chosen to be 10^{-3} and the default PNO occupation number cut-off was 3.33×10^{-7}.

Molecular representations were rendered with *Chemcraft*.[10]

4. *In silico* Structural Search

A computational study of the most plausible structures of each family of anions was carried out to ascertain the most favourable reaction routes taken by the dioxo species. The chosen method was RI-MP2 (see Computational Details) to obtain suitable geometries to enable subsequent single-point energies at the DLPNO-CCSD(T) level.

The RI-MP2 method is a perturbative correction to an unrestricted Hartree-Fock zero order wavefunction which itself may be susceptible to spin contamination when the target low spin electronic state has multiple open shells and cannot be represented by a single Slater determinant. However, if the parent state with the highest m_S value is known (which is always representable by a single Slater determinant), the electronic state energy associated with that microstate can be obtained by the use of spin projection techniques.[11] Inspection of the signs of the local spin densities are then helpful in identifying the spin exchange sites.

4.1. The chemical structure of the $[CeO_2(NO_3)_2]^-$ anion

This cerium anion can only adopt a +III or +IV oxidation state so the number of possible isomers can only be two: An oxo-/-oxyl complex or a peroxo- complex. In the former, the spin density will reside in an oxygen lone pair whereas in the latter it will reside in a 4f orbital. The lowest energy structure corresponds to the one with the alternate oxo-/oxyl- ligands (Table S1).

Table S1 – Relative electronic energies of the optimised structures of the two cerium(IV) structures.

	$\Delta E_{RI\text{-}MP2}$/kJ.mol^{-1}	Total Spin	$\langle S^2 \rangle_{UHF}$	S(S+1)
$[Ce(O)_2(NO_3)_2]^-$	0	½	0.759	¾
$[Ce(\eta^2\text{-}O_2)(NO_3)_2]^-$	+229.4	½	0.751	¾

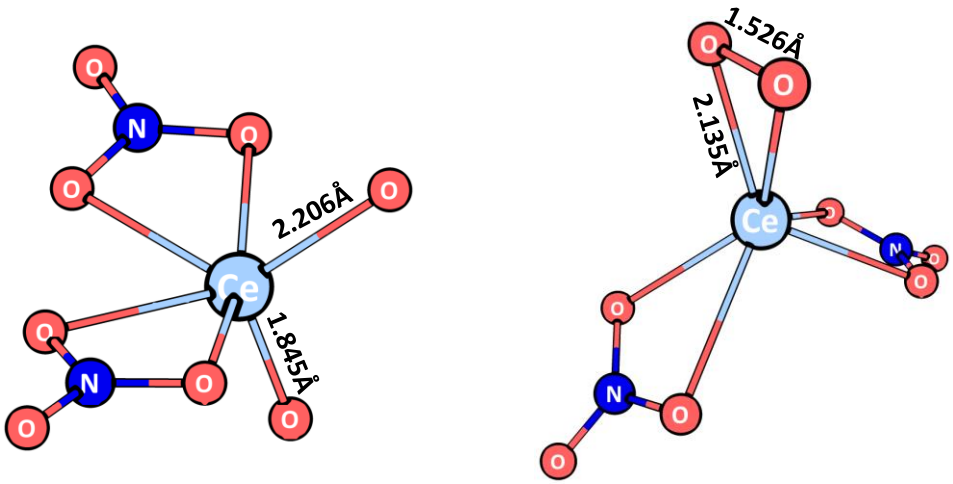

Figure S11 – The geometry of the $[Ce(O)_2(NO_3)_2]^-$ anion (left) and that of $[Ce(\eta^2\text{-}O_2)(NO_3)_2]^-$ (right). Both can only adopt an electronic doublet spin state.

This molecule possesses a short (1.845 Å) Ce=O bond and a longer (2.206 Å) Ce-O• single bond.

4.2. NBO analysis of the $[CeO_2(NO_3)_2]^-$ anion

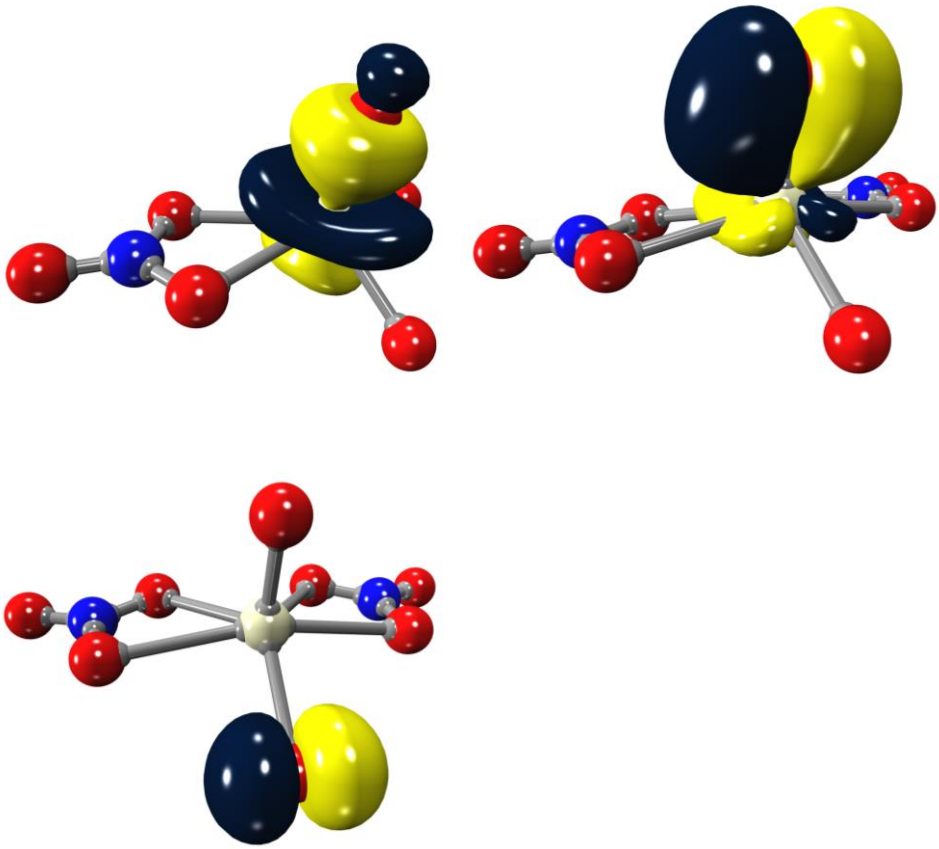

Figure S12 – Natural bond orbitals of $[CeO_2(NO_3)_2]^-$, namely the σ and π cerium oxygen bonds and the lone pair of the oxyl group.

Table S2 – NBO analysis of the $[CeO_2(NO_3)_2]^-$ complex.

Symmetry	Natural Bond Orbital	%Covalency $c_{Ce}/(c_O-c_{Ce})\times100$
σ	17%Ce(5*d*4*f*) + 83%O($sp_\sigma^{2.96}$)	16
π	12%Pr(5*d*4*f*) + 88%O($2p_\pi$)	26

4.3. The chemical structure of the $[PrO_2(NO_3)_2]^-$ anion

With regard to the praseodymium di-oxo anion, since it is an even numbered electron system, the most likely scenarios are given in Scheme S1 - i.e. structure D being a singlet (terminal oxos-) and the remaining A and C triplet (terminal oxo-/oxyl and dihaptic superoxo) or quintet states (B).

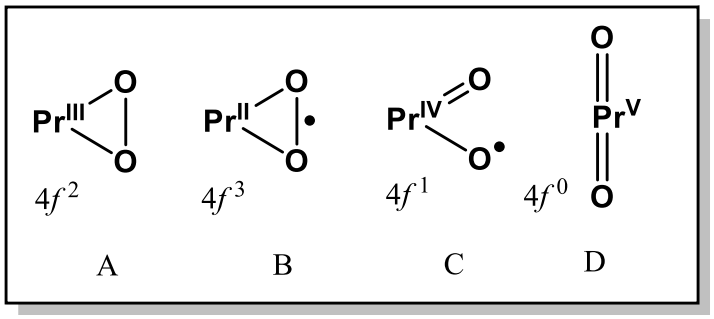

Scheme S1 – Possible bonding scenarios considered for the $[PrO_2(NO_3)_2]^-$ anion.

The relative energies of these optimised structures are displayed in Table S3. The naming scheme given to each structure relates to the bonding situation and multiplicity. In class C, which is of diradical nature, two distinct structures, C.1 and C.2, were obtained, with different multiplicities (S=0 and S=1, respectively). The former is an open shell singlet with spin coupling between the Pr^{IV} and $O^{\bullet}$ sites, the latter is the decoupled analogue. The actual RI-MP2 C.1 minimum is of broken symmetry type (signalled by the spin contaminated $<S^2>$ value) which upon applying spin projection[4] leads to a value of $E_{S=0}$-$E_{S=1}$ =+83.5 kJ/mol.

Table S3 – RI-MP2 optimised structures of $[PrO_2(NO_3)_2]^-$ isomers in several spin states.

Ln=Pr	$\Delta E_{RI\text{-}MP2}$/kJ.mol^{-1}	Total Spin	$<S^2>_{UHF}$	S(S+1)
(D) *trans*-$[Pr(O)_2(NO_3)_2]^-$ (D_{2h})	0	0	0.000	0
(C.1) *cis*-$[Pr(O)_2(NO_3)_2]^-$ (C_2)	+226.2	0	1.061	0
(C.2) *cis*-$[Pr(O)_2(NO_3)_2]^-$ (C_2)	+186.5	1	2.012	2
(A) $[Pr(\eta^2\text{-}O_2)(NO_3)_2]^-$	+276.2	1	2.003	2
(X) $[Pr(\eta^2\text{-}O_2)(NO_3)_2]^-$	(+479.8)	2	6.061	6

The D structure is overwhelmingly the most stable of the ones analysed. The B isomer could not be obtained leading instead to a Pr^{III} distorted structure in which the nitrate has been reduced (Figure S13); this structure is designated by the letter X.

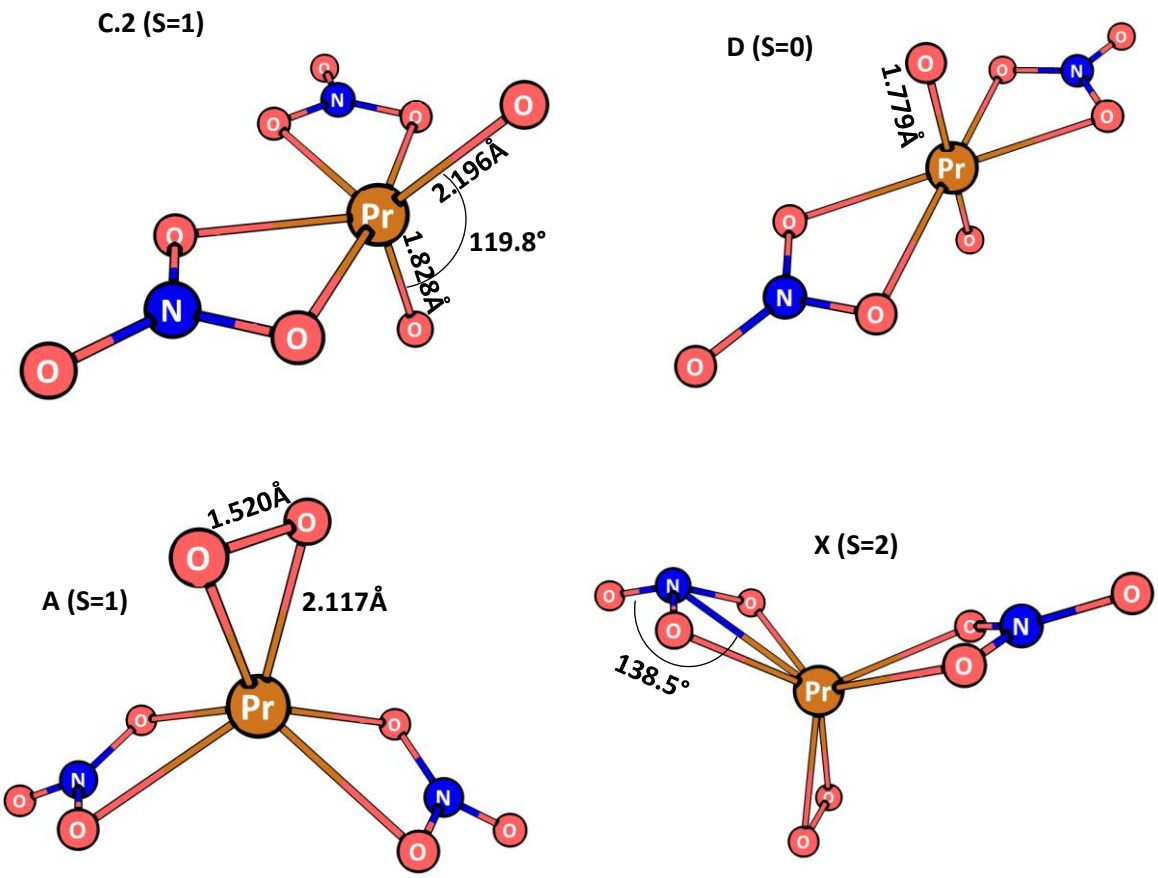

Figure S13 – RI-MP2 optimised structures of praseodymium dioxo-nitrates listed in Table S3.

4.4. NBO analysis of the $[PrO_2(NO_3)_2]^-$ anion

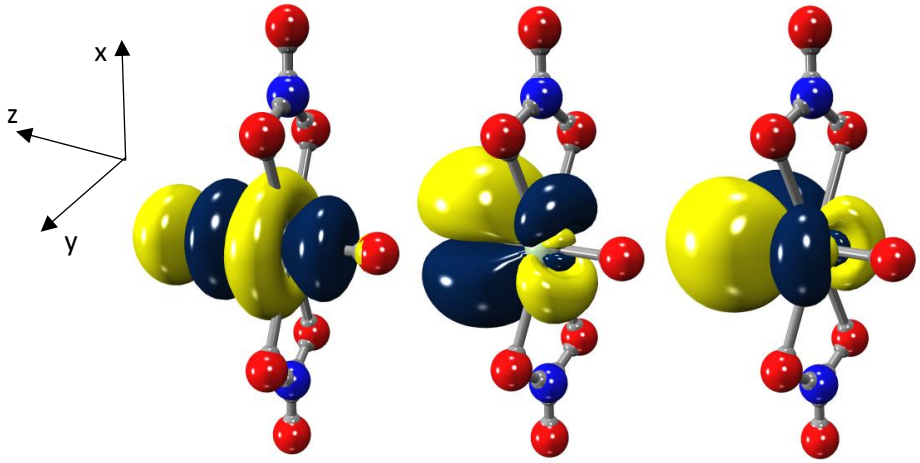

Figure S14 – Natural bond orbitals (NBOs) pertaining to the Pr≡O triple bond.

It may be seen through NBO analysis that the 5*d* orbitals play an equally important role as the 4*f* in the bonding mechanism of the PrO_2^+ fragment.

Table S4 – Natural bond orbital composition of $[PrO_2(NO_3)_2]^-$ featuring 5*d*4*f* natural hybrids on the metal centre.

Symmetry	Natural Bond Orbital	%Covalency $c_{Pr}/(c_O-c_{Pr})\times100$
σ	25%Pr(5*d*4*f*) + 75%O($s_{0.2}p_z$)	50
π_x	19%Pr(5*d*4*f*) + 81%O($2p_x$)	31
π_y	19%Pr(5*d*4*f*) + 81%O($2p_y$)	31

4.5. The chemical structure of the $[NdO_2(NO_3)_2]^-$ anion

By analogy with the previous section, the structures presented in Scheme S2 may be envisaged for the neodymium analogues where simply one more electron is added to the complex. In this case, a search was made for geometries varying from the sextet to doublet states. The latter state would be tantamount to a Nd(V) complex.

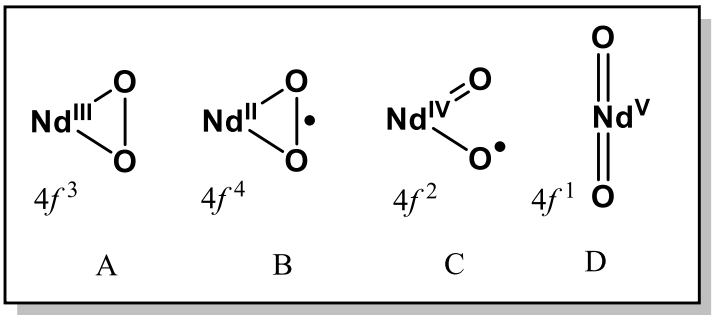

Scheme S2- Possible bonding scenarios for the $[NdO_2(NO_3)_2]^-$ anion.

The RI-MP2 energies of the optimised structures are shown in Table S4 where it may seen that structure type A is lowest in energy corresponding to a di-haptic peroxide species. The Nd(V) isomer was located (D) and lies 208 kJ/mol above the preceding structure. The super-oxide structure (B) is also unstable by 231 kJ.mol^{-1}.

Table S5 – RI-MP2 optimised structures of $[NdO_2(NO_3)_2]^-$ isomers in several spin states.

Ln=Nd	ΔE/kJ.mol^{-1}	S	$\langle S^2 \rangle_{UHF}$	S(S+1)
(C.1) $[Nd(O)_2(NO_3)_2]^-$	+193.3	5/2	8.765	35/4
(C.2) $[Nd(O)_2(NO_3)_2]^-$	+192.0	3/2	4.765	15/4
(C.3) $[Nd(O)_2(NO_3)_2]^-$	+189.0	1/2	2.770	¾
(D) $[Nd(O)_2(NO_3)_2]^-$	+208.2	1/2	0.782	¾
(A) $[Nd(\eta^2\text{-}O_2)(NO_3)_2]^-$	0	3/2	3.754	15/4
(B) $[Nd(\eta^2\text{-}O_2)(NO_3)_2]^-$	+230.8	5/2	8.787	35/4

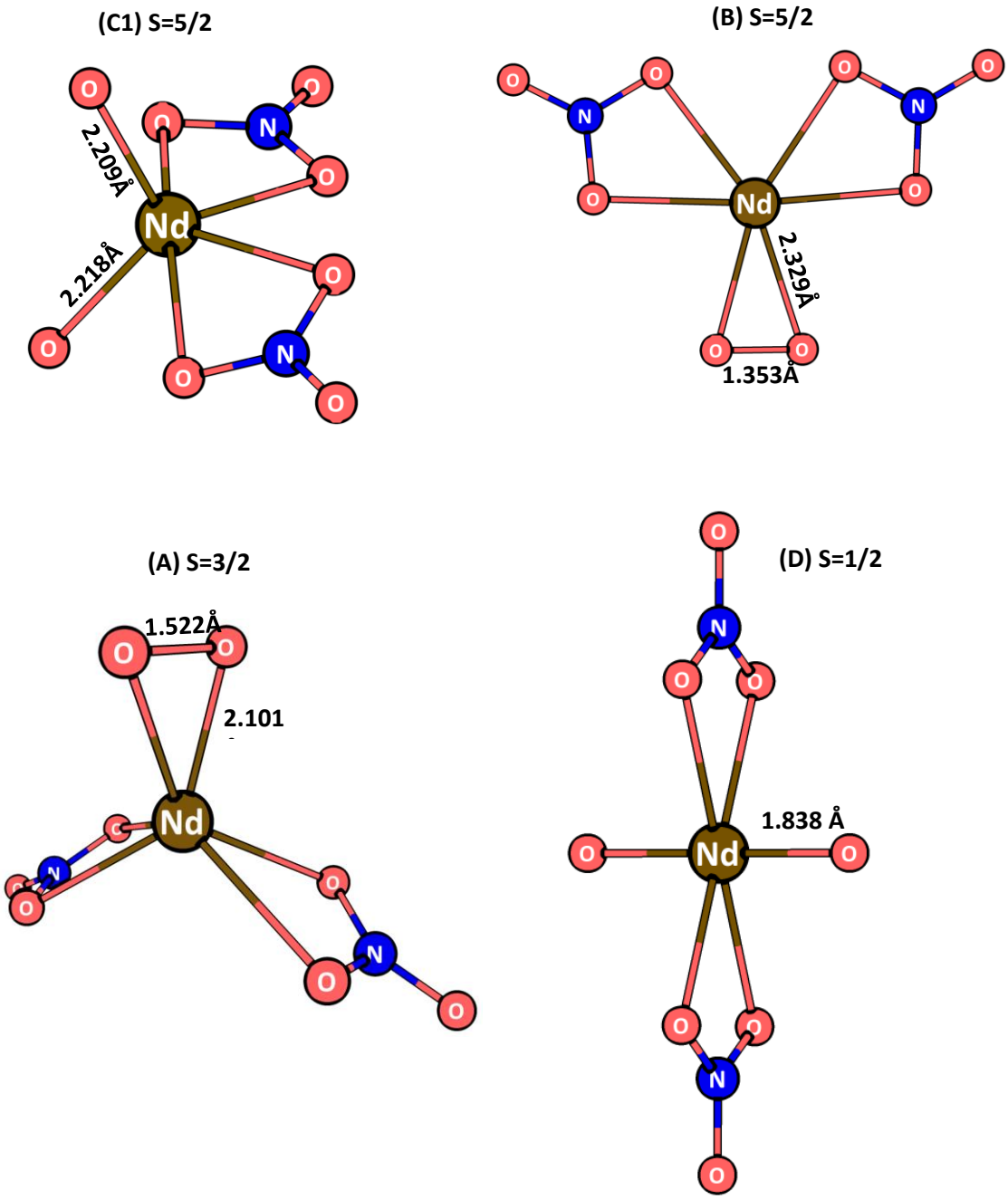

Figure S15 – Optimised geometries of neodymium complexes in several spin states (distances in Å).

Table S6 - Energy differences, maximum amplitudes and T_1 values between different classes of isomers of di-nitrate species.

	RI-MP2	**DLPNO-CCSD(T)**		
	ΔE/kJ.mol^{-1}	ΔE/kJ.mol^{-1}	max. t_{ij}	T_1 diagnostic
$[Ce(O)_2(NO_3)_2]^-$ (S=1/2)	0	0	5.04×10^{-2}	1.84×10^{-2}
$[Ce(\eta^2\text{-}O_2)(NO_3)_2]^-$ (S=1/2)	+229.4	+229.4	8.81×10^{-2}	1.69×10^{-2}
[*trans*-$Pr(O)_2(NO_3)_2]^-$ (S=0)	0	0	6.63×10^{-2}	2.64×10^{-2}
[*cis*-$Pr(O)_2(NO_3)_2]^-$ (S=1)	+186.5	+125.3	5.04×10^{-2}	1.99×10^{-2}
$[Pr(\eta^2\text{-}O_2)(NO_3)_2]^-$ (S=1)	+276.2	+191.7	9.03×10^{-2}	1.79×10^{-2}
$[Nd(\eta^2\text{-}O_2)(NO_3)_2]^-$ (S=3/2)	0	0	8.68×10^{-2}	1.77×10^{-2}
$[Nd(O)_2(NO_3)_2]^-$ (S=5/2)	+193.3	+127.1	5.07×10^{-2}	1.72×10^{-2}
$[Nd(O)_2(NO_3)_2]^-$ (S=1/2)	+208.2	+250.7	4.90×10^{-2}	2.11×10^{-2}

4.6. NBO analysis of the $[NdO_2(NO_3)_2]^-$ anion

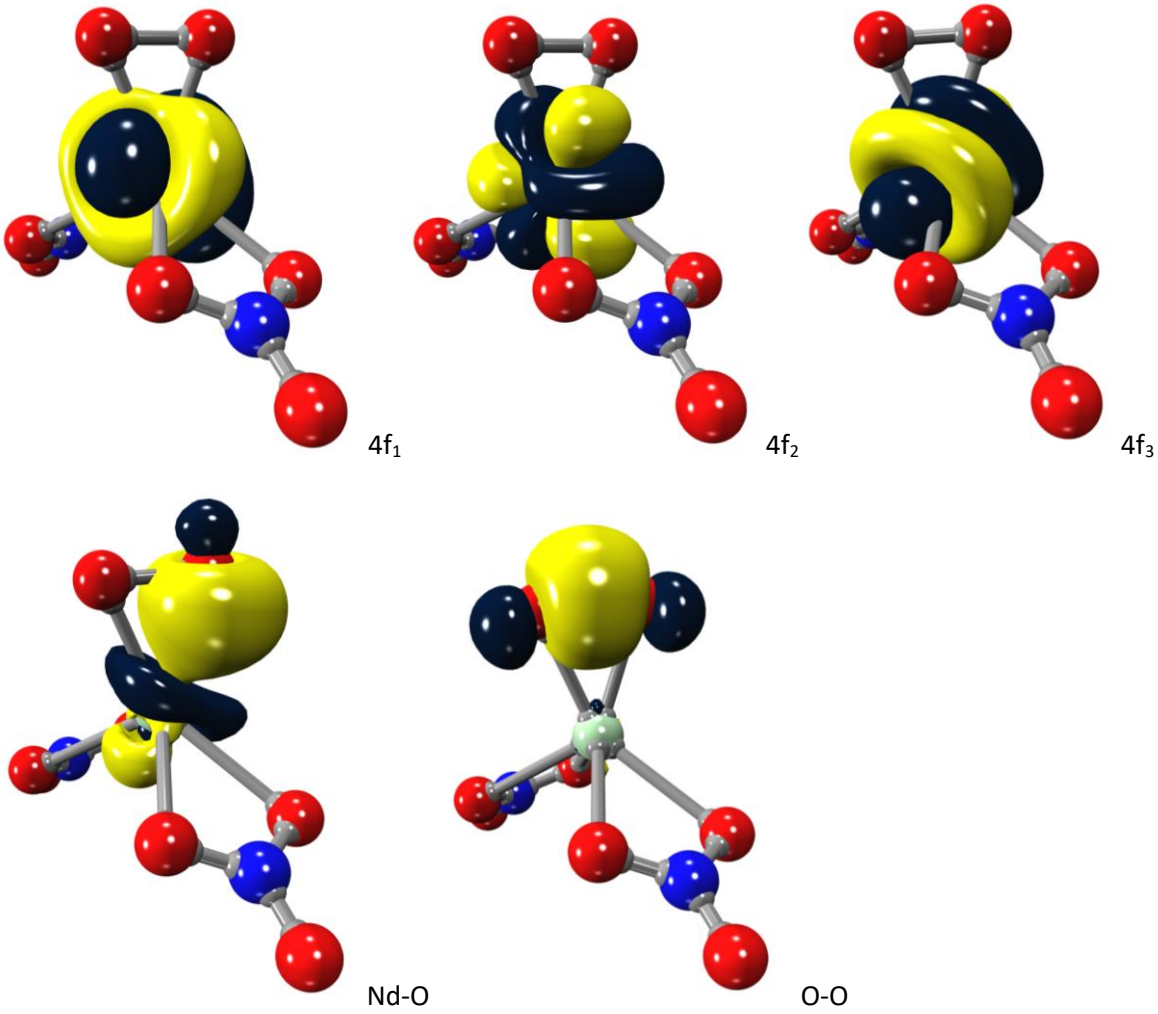

Figure S16 – Natural Bond orbitals of the $[Nd(\eta^2\text{-}O_2)(NO_3)_2]^-$ complex. The three singly occupied 4f orbitals (top) and the Nd-O and O-O bonds (bottom).

Table S7 – Natural bond orbitals of the $[Nd(\eta^2\text{-}O_2)(NO_3)_2]^-$ complex.

	Natural Bond Orbital	%Covalency $c_{Nd}/(c_O\text{-}c_{Nd})\times100$
Nd-O	7%Nd(5*d*4*f*6*s*) + 93%O($s_{0.5}p_\pi$)	8
O-O	50%O(2p) + 50%O(2p)	—

4.7. Reaction outcomes (DLPNO-CCSD(T)/SARC-TZVPP//RI-MP2/SARC-TZVPP)

$$LnO(NO_3)_3^- \xrightarrow{\substack{Ln=Ce,\ \Delta E=+531.2\ kJ\ mol^{-1}\\ Ln=Pr,\ \Delta E=+170.9\ kJ\ mol^{-1}\\ Ln=Nd,\ \Delta E=+35.4\ kJ\ mol^{-1}}} LnO_2(NO_3)_2^- + NO_2$$

$$LnO_2(NO_3)_2^- + H_2O \xrightarrow{\substack{Ln=Ce,\ \Delta E=-0.5\ kJ\ mol^{-1}\\ Ln=Pr,\ \Delta E=+719.1\ kJ\ mol^{-1}\\ Ln=Nd,\ \Delta E=+115.0\ kJ\ mol^{-1}}} LnO_2H(NO_3)_2^- + OH^\bullet$$

4.8. Hydrolysed structures

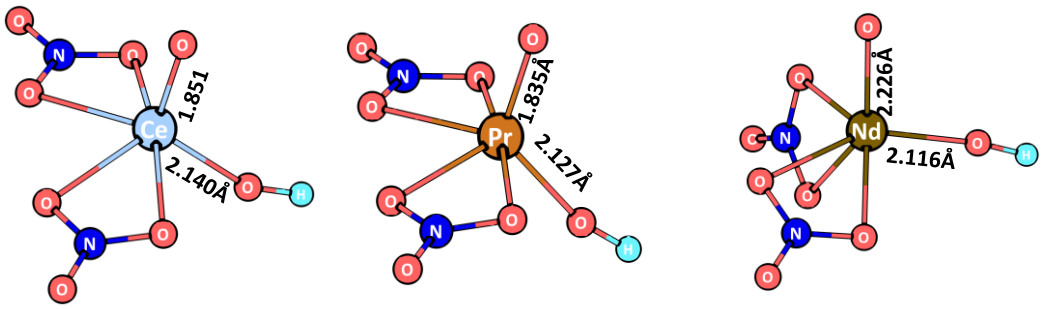

Figure S17 – RI-MP2 optimised structures (distances in Å) of the lowest energy hydrolysis products.

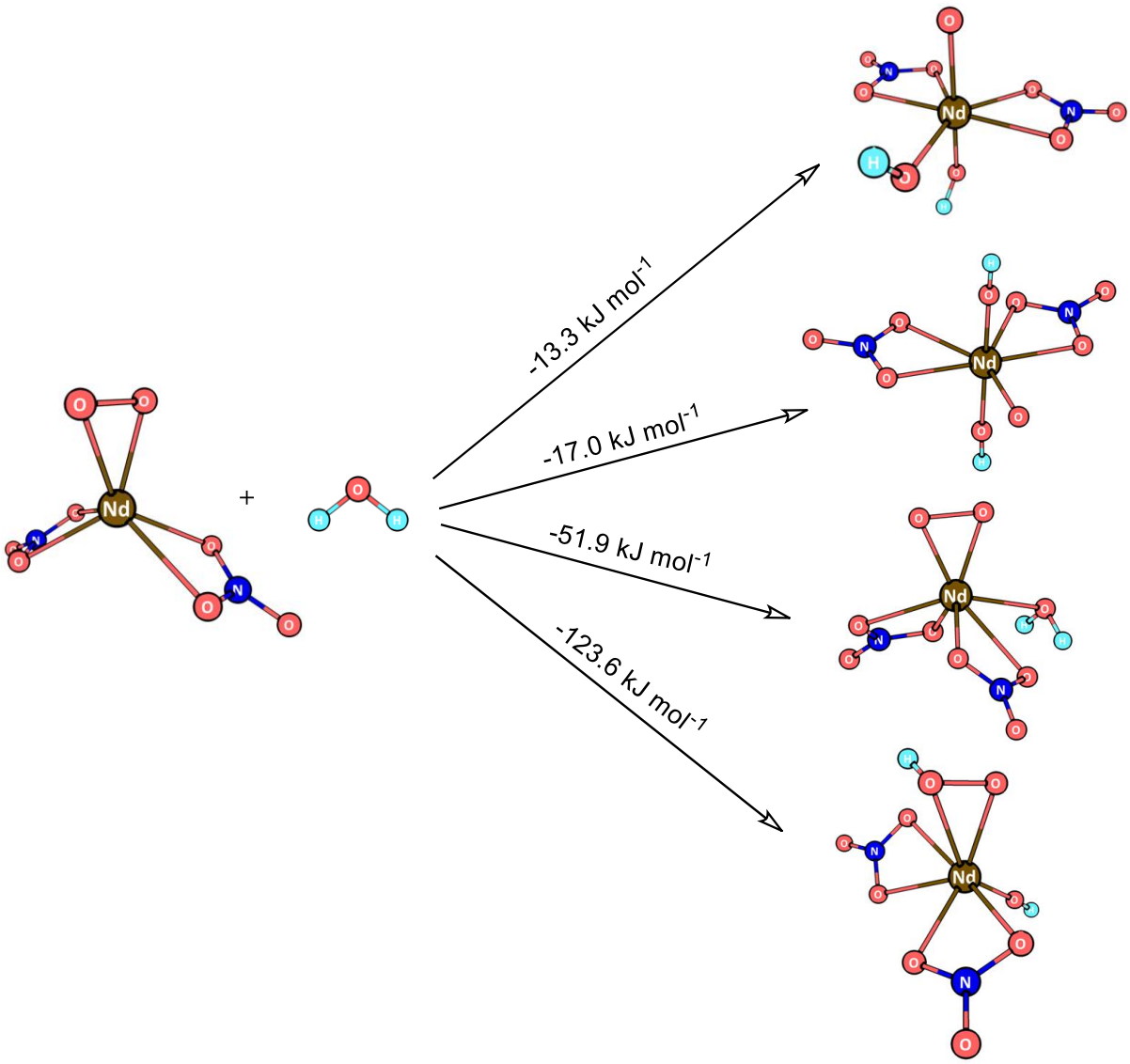

Figure S18 – Reaction outcomes with the general formula $[NdO_3H_2(NO_3)_2]^-$ calculated at the RI-MP2/SARC-TZVPP level.

A data set collection of computational results is available in the ioChem-BD repository[12] and can be accessed via https://doi.org/10.19061/iochem-bd-6-19.

1. Møller C, Plesset MS. Note on an Approximation Treatment for Many-Electron Systems. *Phys Rev* 1934, **46**(7)**:** 618-622.
2. Frank N. An improvement of the resolution of the identity approximation for the formation of the Coulomb matrix. *J Comput Chem* 2003, **24**(14)**:** 1740-1747.
3. Neese F. Software update: the ORCA program system, version 4.0. *Wiley Interdisciplinary Reviews: Computational Molecular Science* 2017, **8:** e1327.
4. Nishino M, Yamanaka S, Yoshioka Y, Yamaguchi K. Theoretical Approaches to Direct Exchange Couplings between Divalent Chromium Ions in Naked Dimers, Tetramers, and Clusters. *J Phys Chem A* 1997, **101**(4)**:** 705-712.
5. Glendening ED, Badenhoop JK, Reed AE, Carpenter JE, Bohmann JA, Morales CM*, et al.* Natural Bond Orbitals program NBO 6.0 ed. Madison, US: University of Wisconsin; 2016.
6. https://github.com/zorkzou/Molden2AIM. Molden2AIM. 2018 [cited]Available from: https://github.com/zorkzou/Molden2AIM
7. Hansen A, Liakos DG, Neese F. Efficient and accurate local single reference correlation methods for high-spin open-shell molecules using pair natural orbitals. *J Chem Phys* 2011, **135**(21)**:** 214102.
8. Sparta M, Neese F. Chemical applications carried out by local pair natural orbital based coupled-cluster methods. *Chem Soc Rev* 2014, **43**(14)**:** 5032-5041.
9. Riplinger C, Pinski P, Becker U, Valeev EF, Neese F. Sparse maps—A systematic infrastructure for reduced-scaling electronic structure methods. II. Linear scaling domain based pair natural orbital coupled cluster theory. *J Chem Phys* 2016, **144**(2)**:** 024109.
10. Zhurko G. Chemcraft 1.8-build 562b. 2019 [cited]Available from: http://www.chemcraftprog.com
11. Ruiz E, Cano J, Alvarez S, Alemany P. Broken symmetry approach to calculation of exchange coupling constants for homobinuclear and heterobinuclear transition metal complexes. *J Comput Chem* 1999, **20**(13)**:** 1391-1400.
12. Álvarez-Moreno M, de Graaf C, Lopez N, Maseras F, Poblet JM, Bo C. Managing the Computational Chemistry Big Data Problem: The ioChem-BD Platform. *J Chem Inf Model* 2015, **55**(1): 95-103.